

Epitaxial growth of high quality InP on Si substrates: The role of InAs/InP quantum dots as effective dislocation filters

Bei Shi¹, Qiang Li¹, and Kei May Lau^{1,*}

¹Department of Electronic and Computer Engineering, Hong Kong University of Science and Technology, Clear Water Bay, Kowloon, Hong Kong

* Tel: (852)23587049, Fax: (852) 23581485, Email: eekmlau@ust.hk

ABSTRACT

Monolithic integration of InP on a Si platform ideally facilitates on-chip light sources in silicon photonic applications. In addition to the well-developed hybrid bonding techniques, the direct epitaxy method is spawning as a more strategic and potentially cost-effective approach to monolithically integrate InP-based telecom lasers. To minimize the unwanted defects within the InP crystal, we explore multiple InAs/InP quantum dots as dislocation filters. High quality InP buffer is thus obtained and the dislocation filtering effects of the quantum dots are directly examined via both plan-view and cross-sectional transmission electron microscopy, along with room-temperature photoluminescence. The defect density on InP surface was reduced to $3 \times 10^8/\text{cm}^2$, providing an improved optical property of active photonic devices on Si substrates. This work offers a novel solution to advance large-scale integration of InP on Si, which is beneficial to silicon-based long-wavelength lasers in telecommunications.

INTRODUCTION

The on-chip light source has always been an indispensable building block in silicon photonics, which normally relies on the heterogeneous integration of III-V active layers on silicon.¹⁻² The hybrid integration approach including wafer bonding technique offers agile solutions to photonic integrated circuits (PICs) with reduced development time.³ However, stringent alignment is usually required and the wafer size is limited by the original III-V substrates. In this regard, monolithic direct epitaxial growth emerges as an attractive alternative to eliminate the high-precision fabrication steps and this approach is naturally suitable for high volume production at a minimum cost.⁴ Recently, the emergence of high performance 1.3 μm quantum dot (QD) lasers motivates the optimization of epitaxial growth of GaAs on Si with low dislocation density.⁵⁻⁸ Yet, for multi-channel wavelength division multiplexing (WDM) in long-haul telecommunications, photonic devices are mostly fabricated on the basis of InP and its related alloys. Although efforts devoted to growing high quality InP-on-Si (IoS) compliant substrates originated since the 1980s,^{9,10} progress is still hindered by the 8% high lattice mismatch, twice the misfit of GaAs/Si. Consequently, the most serious issue in heteroepitaxy is the high density of defects, including threading dislocations (TDs), stacking faults (SFs), twins, and anti-phase boundaries (APBs).¹¹ To alleviate this problem, various techniques have been attempted - selective-area growth (SAG),¹²⁻¹³ epitaxial lateral overgrowth (ELOG),¹⁴ adopting compositional graded/intermediate buffers,¹⁵⁻¹⁶ inserting two-dimensional (2D) strained interlayers or superlattices (SLs),¹⁷⁻¹⁸ and applying a thermal cycle annealing process,⁹ to name a few.

Previously, we adopted self-assembled InAs/InAlGaAs QDs system as the dislocation filter layers (DFLs),¹¹ and reported on the effectiveness. In this article, the QD DFLs are

systematically optimized to further improve the InP crystalline quality. By replacing the InAlGaAs alloy with a InP cap layer, the growth front of InP buffer can be smoothed prior to each subsequent QD layer. As a consequence, the surface of the IoS substrate is much smoother with a root-mean-square (RMS) value of only 2.88 nm across a scanning area of $10 \times 10 \mu\text{m}^2$. The dislocation filtering effect was examined by statistical plan-view and cross-sectional transmission electron microscopy (PV-TEM and XTEM) approaches, revealing a reduced defect density of $3 \times 10^8/\text{cm}^2$. To further evaluate the optical properties of the IoS templates, a single layer of InAs/InAlGaAs QDs sandwiched by InAlGaAs claddings was deposited on the InP buffers and an evidently improved photoluminescence (PL) emission was achieved based on the optimized InP buffer with the optimized InAs/InP QD dislocation filters.

II. EXPERIMENTAL SECTION

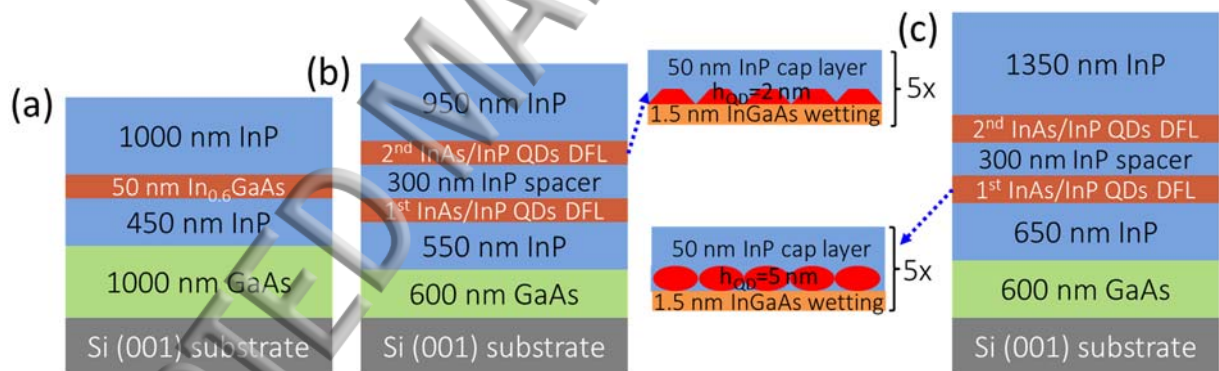


FIG. 1. Schematic illustration of InP grown on planar Si with (a) a single strained InGaAs interlayer, and two periods of 5-layer InAs/InP QD DFLs with a dot height of (b) 2 nm, and (c) 5 nm, respectively.

Figure 1 illustrates the schematic of three samples compared in this study. All the material growth was completed on 4-inch nominal (001) silicon substrates using an Aixtron AIX-200/4 metal-organic chemical vapor deposition (MOCVD) system. Prior to III-V material growth, the silicon substrates were cleaned by a standard RCA-1 solution and then thermally annealed at

800 °C for oxide desorption. For the epitaxial growth of InP on Si substrates, a GaAs intermediate buffer was adopted to accommodate the lattice mismatch.¹⁶ The GaAs buffer consists of a 10-nm-thick low-temperature (LT) GaAs nucleation at 400 °C with a low growth rate of 1.5 nm/min, a moderate-temperature (MT) buffer at 550 °C to smooth the growth front with growth rate gradually increasing from 2.4 to 15 nm/min, and finally, a thick high-temperature (HT) layer at 600-630 °C to acquire good material quality with a fast deposition rate of 30 nm/min. The growth procedures for the InP buffer are exactly the same as the GaAs, except for a slightly higher nucleation temperature at 435 °C. In sample A, a standard structure with 1.5 μm InP (inserted with a 50-nm-thick single strained In_{0.58}Ga_{0.42}As interlayer) grown on the 1-μm-thick GaAs buffer, serving as a reference. For sample B and C, two periods of 5-layer InAs/InP QDs were introduced during the HT-InP layer growth, separated by 300 nm HT-InP spacer. The InAs/InP QD filters began with the deposition of a 1.5 nm In_{0.45}Ga_{0.55}As wetting layer, followed by 3.6 monolayer (ML) InAs QDs growth at 510 °C with a rate of 0.4 ML/s and an effective V/III ratio of 0.4. After a 25s growth interruption (GRI) without any arsenic injection, the LT-InP first capping layer (FCL) was deposited at the same temperature as QDs and a growth rate of 0.8 ML/s. Subsequently, the temperature was ramped up to 600 °C for the HT-InP second capping layer (SCL). The temperature profiles for samples A and C are summarized in Fig. 2.

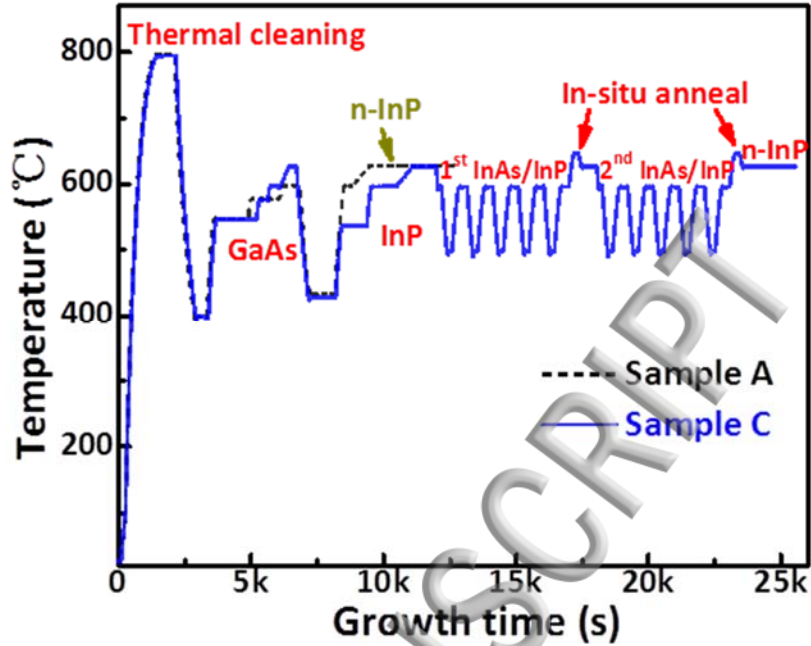


FIG. 2. Schematic showing the detailed InP-on-Si growth procedure of samples A and C.

The difference between samples B and C mainly lies in the height and morphology of the QDs, achieved by varying the deposition thickness of the LT-InP cap layer ($h=2$ nm for sample B, and 5 nm for sample C). The basic information about the three grown samples is summarized in Tab. 1.

TAB. 1. Summary of the three as-grown samples.

Sample	Dislocation filter materials	Buffer thickness (μm)	Defect density (PV-TEM)	Roughness ($10 \times 10 \mu\text{m}^2$)
A	50 nm strained $\text{In}_{0.6}\text{Ga}_{0.4}\text{As}$ interlayer	1 μm GaAs + 1.5 μm InP	$1.2 \times 10^9/\text{cm}^2$	4.60 nm
B	Two periods of multiple InAs/InP QDs ($h_{\text{QD}}=2$ nm)	0.6 μm GaAs + 1.5 μm InP	$5.5 \times 10^8/\text{cm}^2$	2.56 nm
C	Two periods of multiple InAs/InP QDs ($h_{\text{QD}}=5$ nm)	0.6 μm GaAs + 2.8 μm InP	$3.0 \times 10^8/\text{cm}^2$	2.88 nm

RESULTS AND DISCUSSION

A. Effects of InP spacer

Figure 3(a) depicts the cross-sectional scanning electron microscope (X-SEM) image of sample A. To better reveal the morphology of the inserted InGaAs layer, sample A was wet-etched in a H_3PO_4 -based solution prior to SEM characterization. It is noted that the inserted InGaAs ternary alloy was quite bumpy and the thickness fluctuates. This is probably due to the rough InP growth front and the compositional disorder of InGaAs ternary alloy. By further capping the InGaAs with the binary InP, the surface can be smoothed again. For sample B and C, InAs/InP QD DFLs were applied, and the InP DFL separator was fixed at 300 nm in order to obtain a smoother surface before the subsequent QD stack growth. Figure 3(b), an X-SEM image of sample C, shows no surface undulation. This favors a uniform QDs distribution and prevents the formation of defective InAs coalesced islands. In this case, a better dislocation filtering effect can be anticipated.

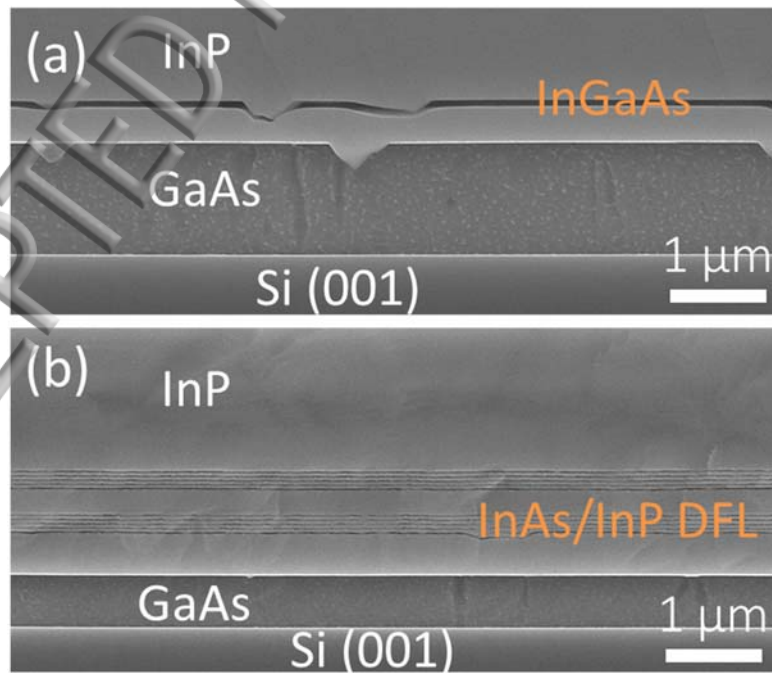


FIG. 3. Cross-sectional SEM images of (a) InP on planar Si with a single InGaAs interlayer, and (b) InP on planar Si inserted with two periods of 5-layer InAs/InP QD DFLs.

Figure 4 displays a typical $10 \times 10 \mu\text{m}^2$ atomic force microscopy (AFM) scan of sample A and C respectively. A smoother InP surface with an RMS value of only 2.88 nm was achieved for sample C, as a result of the multiple InAs/InP QDs insertion. The density of pinholes is significantly reduced on the surface of sample C, suggesting lower TDs on the InP top surface.¹⁹ The SFs manifested themselves as short dashed lines on the AFM images, as revealed in Fig. 4(b).

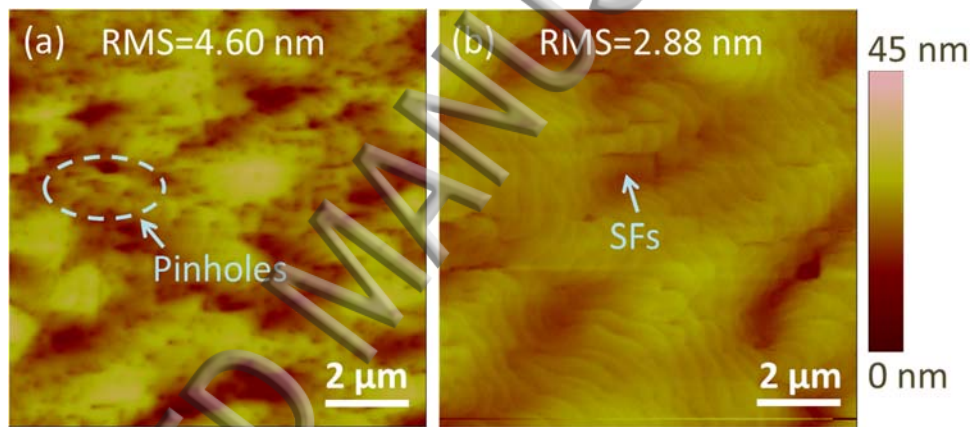


FIG. 4. Typical $10 \times 10 \mu\text{m}^2$ AFM images of InP-on-Si surface (a) without and (b) with QD dislocation filters. The RMS values for these two samples are 4.60 nm and 2.88 nm, respectively.

B. Defect characterization

X-ray diffraction (XRD) ω -rocking and ω - 2θ scans were performed separately to compare the InP quality and evaluate the effect of InAs/InP dislocation filters. Figure 5(a) overlays the x-ray spectra of the three samples. The relative intensity difference between InP and GaAs is mainly associated with their deposited layer thicknesses. Satellite peaks are clearly identified for samples B and C, correlated to the embedded InAs/InP QDs. The distinct satellite peaks with

higher orders in sample C indicate smoother interfaces of the InAs/InP QDs. The shoulder in sample A is related to the InGaAs insertion layer, matching the indium compositions. The full-width at half-maximum (FWHM) of the InP main peak directly reflects the material quality of the InP buffer, which has been plotted in a linear scale in Fig. 5(b). The InP peak in sample C is evidently sharper and narrower, revealing an improved buffer quality after the optimized QDs have been inserted. This observation is further verified by the ω -rocking scan, as presented in Fig. 5(c). The spectrum broadening of the InP buffer after QD insertion is less severe, and according to Ayers' model,²⁰ the defect density can be estimated by:

$$D = \frac{\beta^2}{4.36b^2} \quad (1)$$

where β is the FWHM of the XRD ω -rocking scan in radians and b is the magnitude of burger's vector (for 60° dislocation on InP, $b=a/\sqrt{2}=4.15\text{\AA}$, and $a=5.8688\text{\AA}$ is the lattice constant of InP). Considering that XRD is measuring a wide area of the sample and the x-ray can penetrate into a depth of up to several μm , the values obtained here reflect an upper bound of the defect density, which are 1.74×10^9 , 1.43×10^9 , and $8 \times 10^8 \text{ cm}^{-2}$ for sample A, B, and C, respectively.

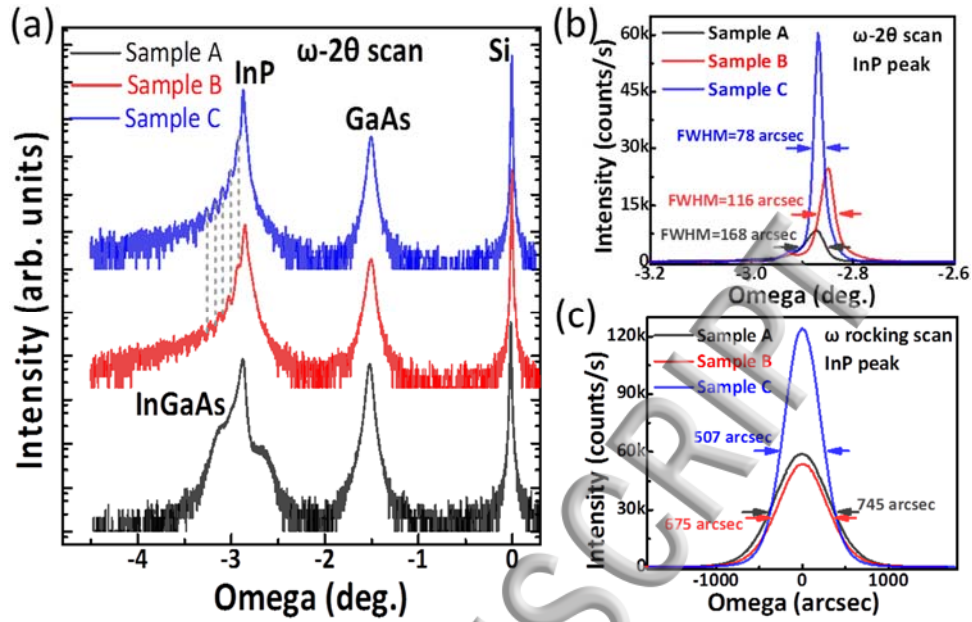


FIG. 5. (a) XRD ω - 2θ scan of the three samples and (b) zoomed-in linear plot of the ω - 2θ curves around the InP peak; and (c) ω -rocking scan of the three samples.

To directly monitor the generation and propagation of the defects in detail, cross-sectional TEM lamellas of these three samples were further prepared. Figure 6(a) presents a global view of sample A. Figures 6(b) and 6(c) show that the defects originate from the hetero-interface of the GaAs/Si and InP/GaAs. Compared with the dislocations in the GaAs intermediate buffer, a much higher density of defects in the InP buffer are generated from the InP/GaAs interface, as shown in Fig. 6(a). The strained InGaAs layer can partially bend the dislocations towards the edge of the sample (Fig. 6(d)), contributing to the dislocation annihilation. Nevertheless, still a considerable number of TDs can penetrate through the InGaAs layer and the defect density terminating at the top surface is determined to be $1.2 \times 10^9/\text{cm}^2$ on average according to the PV-TEM images shown in Fig. 9(a).

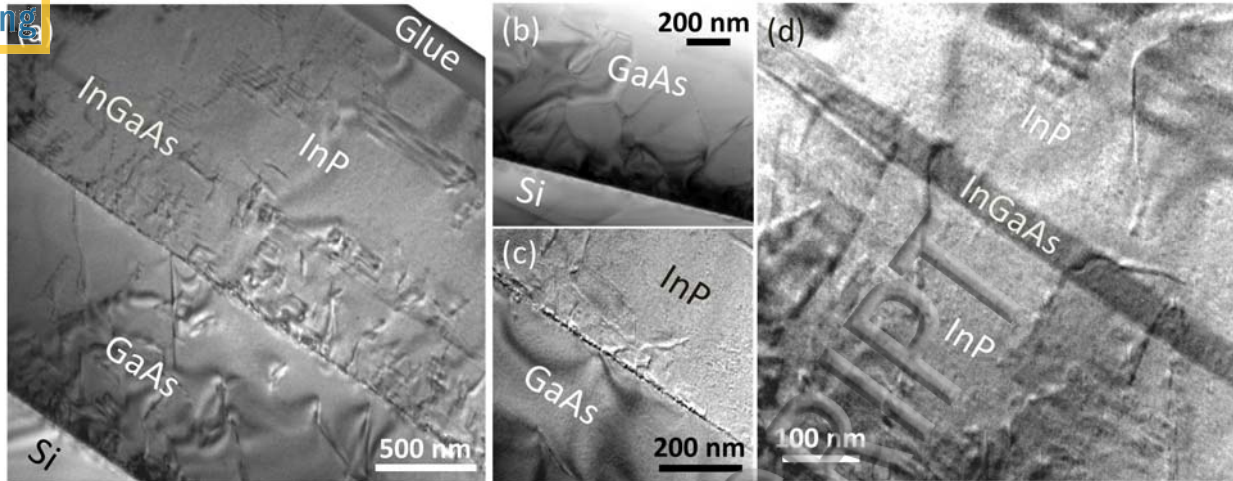


FIG. 6. Cross-sectional TEM images of (a) InP on planar Si with a single InGaAs interlayer and GaAs intermediate buffer. Zoomed-in observation of (b) GaAs/Si and (c) InP/GaAs hetero-interfaces. (d) Close-up view of the TDs bent by the InGaAs strained layer.

For sample B inserted with 2 nm height QD DFLs (Fig. 7(a)), although the dislocations can be influenced by the QDs, sufficient defects can still propagate upward to the top surface, especially the SFs. These SFs appear as short dashed lines in the plan-view TEM images in Fig. 9(b). Comparing the TEM images of samples B and C in Fig. 7, the dislocation filtering efficiency of the 2 nm high QDs is clearly lower than the 5 nm high QD DFLs in sample C.

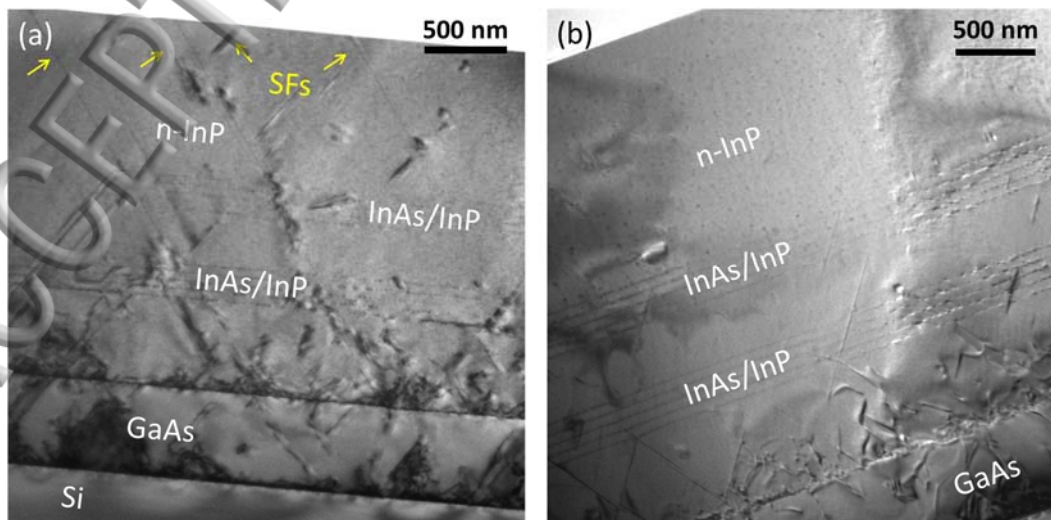


Fig. 7. Cross-sectional TEM images of InP on planar Si with (a) 2 nm and (b) 5 nm height QD DFLs.

Very few TDs can be detected above the second stage of QD DFLs in sample C, and most of the defects are propelled or pinned by the stacked QDs, leading to either annihilation or coalescence of the TDs, as demonstrated in Fig. 8(a). Figure 8(b) shows a close-up view of the 5 nm high multiple QD stacks. The vertical mis-alignment of the QDs offers a more sufficient interaction of dislocations with the QDs. With a closer inspection, a single QD is identified, showing a diameter of 30 nm and a height of 5 nm. The darker region surrounding the QDs represents the strain field of an InAs QD. Figure 8(d) illustrates an example of 60° mixed dislocations bent by the base of the QDs. Additionally, for edge dislocations that are only slightly influenced by the 2D strained superlattices, they can be terminated at the surface of 3D QDs.⁶ However, we also observe some TDs and SFs penetrating through the DFLs across certain regions of sample C. Worse still, these defects result in a rougher InP growth front, which accelerates the nucleation of large InAs islands and indium adatoms aggregation. As shown in Fig. 8(e), the lengthy defects degrade a fraction of the QD DFLs and it is challenging to resolve this issue. A promising solution is to apply thermal cycle annealing or post-annealing methods after each stage of QDs growth to thermally propel the dislocations from propagating towards the subsequent QD DFLs. Yet, the annealing temperature has to be carefully optimized.

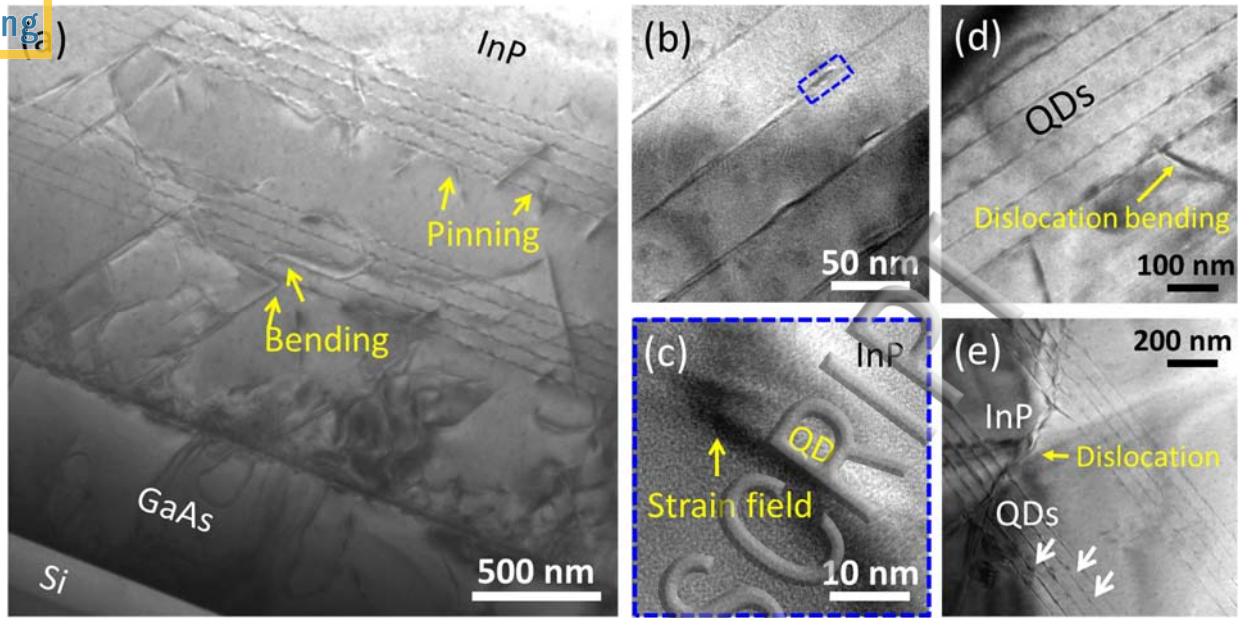


FIG. 8. Cross-sectional TEM images of (a) InP on Si inserted with 10 layers of 5 nm-in-height QD DFLs. (b) Close-up view of the QD stacks. (c) High resolution TEM showing a single QD. (d) A 60° dislocation bent by the base of the QDs. (e) Lengthy threading dislocations penetrating through the QD stacks.

Figure 9 presents the PV-TEM images of the three samples to accurately quantify the dislocation densities that terminate at the InP top surface. The defect density (including TDs and SFs) was determined by counting the number of defects within a given area of $1.93 \times 1.93 \mu\text{m}^2$, based on an average number of 10 PV-TEM images for accuracy. Figures 9(a)-(c) present three typical PV-TEM images at various regions for sample A to C, respectively. In addition to a gradual decrease of defect density from $1.2 \times 10^9 \text{ cm}^{-2}$ in sample A to $3 \times 10^8 \text{ cm}^{-2}$ in sample C, as summarized in Tab. 1, the SFs density is also clearly minimized for the sample with higher QD DFLs upon comparing samples B and C. This suggests that the DFLs with a larger QD height are much more efficient in filtering TDs as well as SFs.

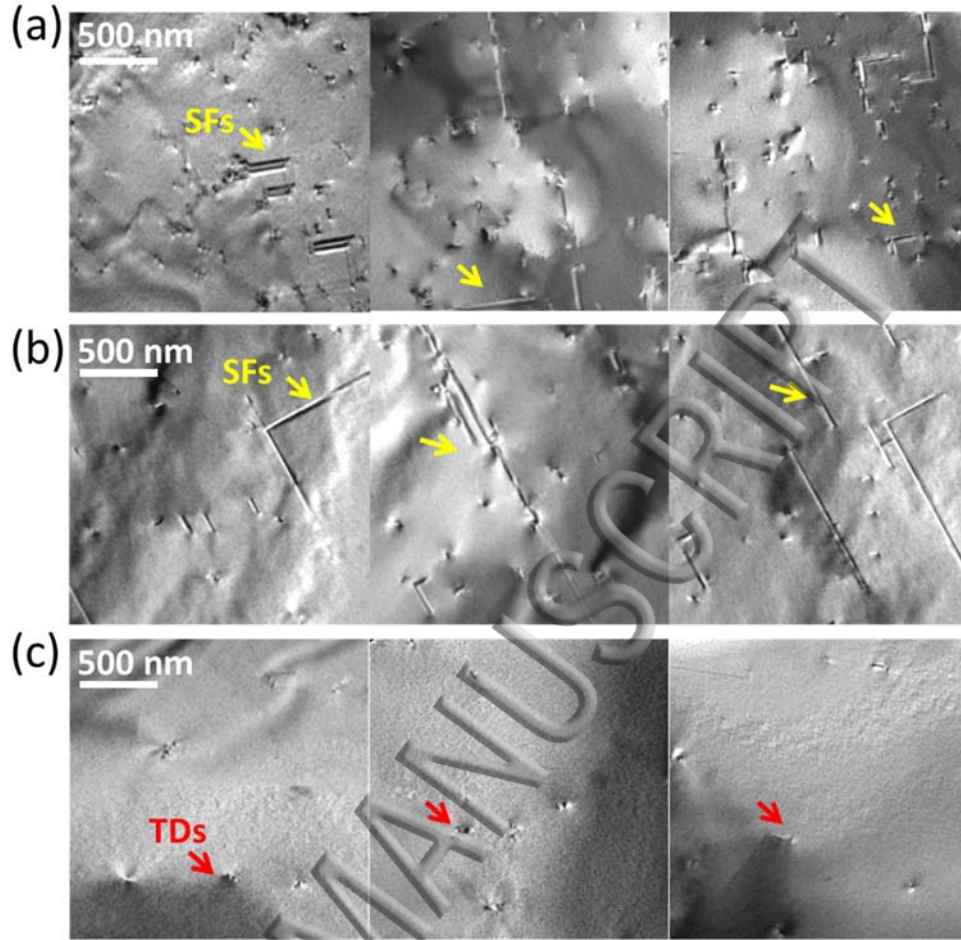


FIG. 9. Plan-view TEM images of (a) sample A of 1.5 μm InP on planar Si with a single InGaAs strained interlayer, (b) sample B of 2.3 μm InP on planar Si with 2 nm in height InAs/InP QD DFLs, and (c) sample C of 2.8 μm InP on planar Si with 5 nm in height InAs/InP QD DFLs (SFs and TDs are identified in different colors).

C. Dislocation filtering analysis

The best dislocation filtering effects observed in sample C can be explained as follows: Theoretically, assuming all coherently strained islands (i.e., QDs) are smaller than the critical size, no dislocations shall be generated by the QDs themselves. Then, bending of dislocations will occur when ΔE_{rel} (strain energy released due to misfit dislocation generation) is equal or

larger than ΔE_{dis} (dislocation self-energy). According to the modeling,²¹ ΔE_{rel} and ΔE_{dis} can be expressed as:

$$\frac{\Delta E_{\text{rel}}}{L} = \frac{2G_{\text{dot}}(1+\nu)}{(1-\nu)} f_{\text{eff}} b_{\text{eff}} h \quad (2)$$

$$\frac{\Delta E_{\text{dis}}}{L} = \frac{1}{2\pi} \frac{G_{\text{buff}} G_{\text{dot}}}{G_{\text{buff}} + G_{\text{dot}}} b^2 \left(\frac{1-\nu \cos^2 \beta}{1-\nu} \right) \left[\ln \left(\frac{2r}{b} \right) + 1 \right] \quad (3)$$

Here in the expressions, L is the length of the misfit dislocation, G_{dot} and G_{buff} are the shear modulus of the QDs and buffer layer respectively, ν is the Poisson ratio, $f_{\text{eff}} = f\sqrt{1 - \exp(-\kappa/p)}$ is the effective lattice mismatch between the QD and the underlying buffer layer (where f is the lattice mismatch between the QDs and buffer, $\kappa \approx 0.09$ and $p = H/W \approx H/L$, which is the height-width ratio of a truncated QD). The misfit dislocation length is comparable with the base width of a QD ($L \approx W$). b_{eff} is the Burger's vector component parallel to the dot-buffer layer interface, and β is the angle between Burger's vector and the dislocation line. h and r are functions of x , which is the distance from the dislocation bent point to the center of the QD.

TAB. 2. Parameters for InAs/InP quantum dot system.

Material	Lattice mismatch (f)	Poisson ratio (ν)	Shear modulus of QDs (G_{dot})	Shear modulus of buffer (G_{buffer})	Burger's vector (b)	Burger's vector angle (β)	Average QD base width (W)
InAs/InP	3.1%	0.36	31.2 GPa	61.1 GPa	4.15 Å	60°	~40 nm

The parameters for the InAs/InP QD system are derived and summarized in Tab. 2 based on published database.²¹ When $\Delta E_{\text{rel}} \geq \Delta E_{\text{dis}}$, these parameters can be substituted into the formula for calculation. For the base width of InAs/InP QDs, it is normally in the range of 30 nm~45 nm

(taking the average value of 40 nm in our case), thus the dot height should be at least 4 nm to possess the effective dislocation filtering function. Here, the height of these buried QDs is limited by the thickness of the LT-InP cap layer. Therefore, the dislocation filtering efficiency of sample C (buried dot height of 5 nm) is better than sample B (buried dot height of 2 nm).

As for the influence of the QD density, the trend is consistent with InAs/GaAs dislocation filters.⁶ It is anticipated that a larger QD with a higher dot density is preferred for dislocation filtering. Here, the QD density is about $3 \times 10^{10}/\text{cm}^2$, a typical value for the InAs/InP QDs system.²²⁻²³ It was also uncovered that a higher QD density can be achieved by stacking the InAs/InP QDs.²⁴ Moreover, more quantum dot stacks can facilitate the interaction of dislocations and the strain field of the QDs, enhancing the bending effect of propagated dislocations. However, over stacking of QDs will lead to strain accumulation and the excessive strain may get released by generating new threading dislocations. Since this is a strain-dependent analysis, to simplify our case, we can refer to the InAs/GaAs example. For the InAs/GaAs with a larger lattice mismatch ($\sim 7\%$), the critical layer number reported is 10~15,²¹ while for the lattice mismatch of InAs/InP QD dislocation filters ($\sim 3.1\%$), the critical layer number should be larger than 20. However, considering the growth period and managing the total buffer thickness, we only grew 2 periods of 5-stack QDs (10 QD layers in total) in samples B and C. For future improvements of the grown structure, increasing the QD stack number inside the InP buffer can be taken into consideration.

D. Optical properties

To directly examine the potential of these templates for future silicon-based QD laser applications, a single InAs/InAlGaAs QD active layer was deposited on the three InP-on-Si

samples. The single sheet QDs were sandwiched by two 200 nm HT-InAlGaAs claddings, and another layer of uncapped InAs QDs sharing the identical QD growth conditions was deposited atop for AFM investigation, as presented in Figs. 10(b) and 10(d). For the InAlGaAs capping process, a 1.3 nm thin LT-InAlGaAs (510 °C, growth rate of 10 nm/min) was first deposited, followed by the HT-InAlGaAs at 630 °C. The diagram of the structure is illustrated in Fig. 10(a). The as-grown samples were then characterized by a RT- μ PL setup under two different excitation regimes for the evaluation of QD densities and optical properties, respectively.

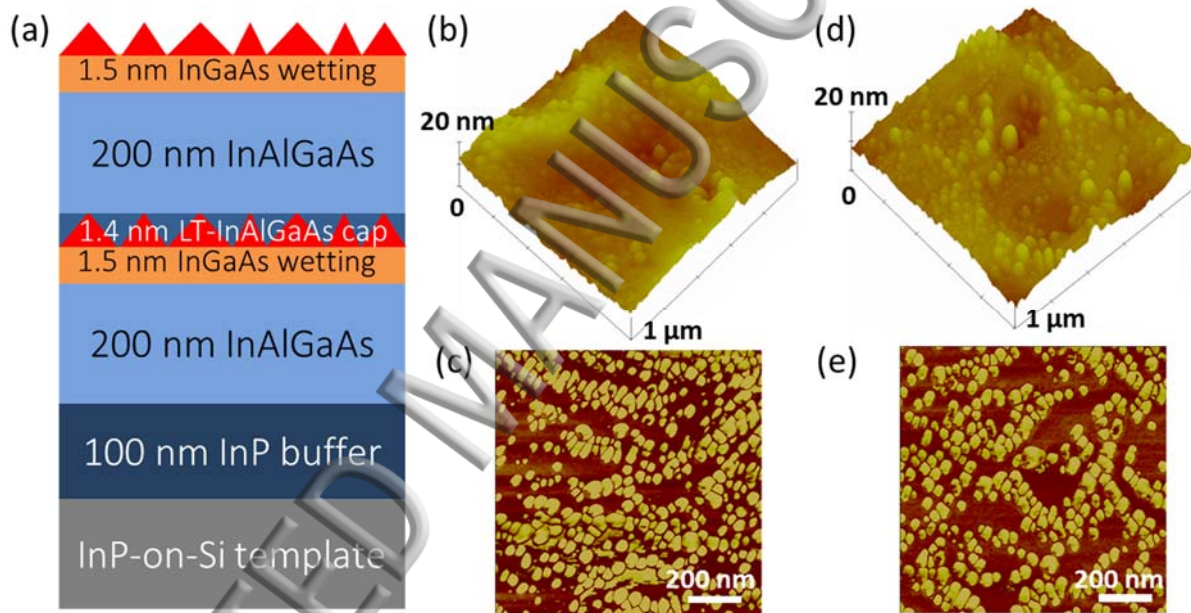


FIG. 10. (a) Schematic diagram of uncapped QDs on single sheet InAs/InAlGaAs grown on the three InP-on-Si templates. Typical three-dimensional $1 \times 1 \mu\text{m}^2$ AFM amplitude and phase diagrams of uncapped single layer of InAs/InAlGaAs QDs grown on (b, c) sample A and (d, e) sample C, respectively.

The quantum dot densities are counted from the corresponding AFM phase diagrams shown in Figs. 10(c) and 10(e). The dot densities for samples A and C are $3.4 \times 10^{10} \text{cm}^{-2}$ and $3 \times 10^{10} \text{cm}^{-2}$, respectively. The difference is further supported by the RT power-dependent PL in Fig. 11. Due

Due to the slightly higher dot density on sample A, the PL intensity difference between samples A and C is smaller at a higher excitation regime.

According to the measured spectra in Fig. 11, the single layer QDs grown on sample C exhibits the highest peak intensities at both pumping powers, indicating minimum defects inside the single layer of QDs active region. The defects originate from both the InP-on-Si template and the active region. The broad spectrum for single layer QDs on sample C with a relatively larger linewidth of 136 meV is due to the large inhomogeneity of the QDs, and a bimodal distribution of the QD sizes.²⁵ The bimodal distribution also occurs in samples A and B, with two peaks clearly identified. At RT, the photoluminescence from the two branches of QDs get overlapped, broadening the spectrum. A visible transition from the main peak to the shoulder on the higher energy side is also noted for high power excitation (4 kW/cm^2). This transition originates from the bimodal distribution of QD sizes. The longer wavelength peak corresponds to the relatively larger QD branches. At RT, the larger QDs dominate the luminescence for two reasons: First, the carrier capture efficiency for larger QDs is higher, compared to the smaller QDs.²⁶ Secondly, the thermally assisted tunneling of carriers via coupled excited states (CES) contribute to the charge carrier transfer to the larger QDs from the smaller ones.²⁷ However, in high excitation regime, the excessive carriers can still easily diffuse into the smaller QDs to enhance the shorter wavelength PL emission.

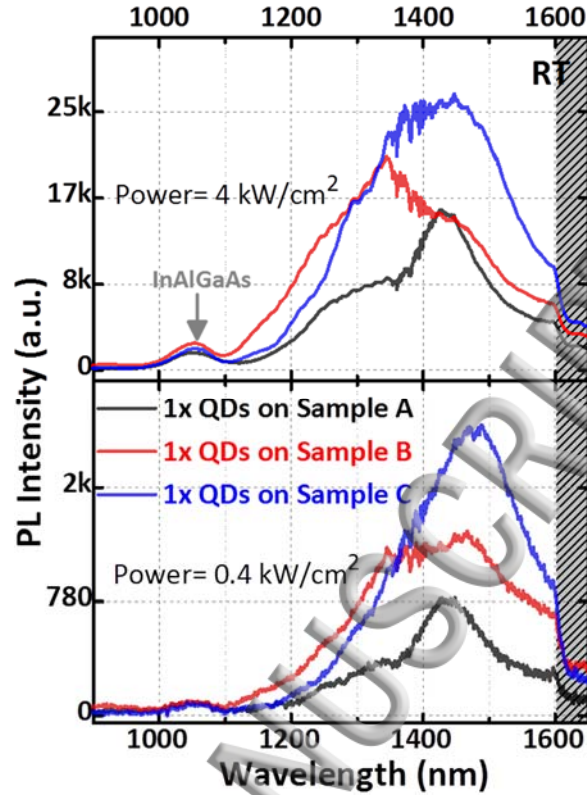


FIG. 11. RT- μ PL spectra of single sheet InAs/InAlGaAs QDs on top of the three samples under two different excitation regimes (spectra cutoff beyond 1600 nm).

In addition to RT-PL characterization, the temperature-dependent PL is carried out to study the internal quantum efficiencies (IQEs) and the activation energies of single layer QDs on the three IoPS templates. The IQE at RT can be calculated based on the ratio of integrated PL at RT to the highest integrated PL intensity at low temperatures^{18,28}

$$\eta_i = I_{PL}(T = 296K)/I_{PL}(T = 20K) \quad (4)$$

The integrated PL intensity (IPLI) as a function of temperature has been summarized and plotted in Fig. 12(b). The calculated IQE values for the samples A-C are 12.2%, 13.7%, and 17.3%, respectively. To further improve the IQE value, efforts should be devoted to optimizing the QDs growth condition, minimizing the defect density and improving the surface smoothness

of the IoPS templates. Still, the relatively higher IQE for QDs on sample C directly suggests a lower dislocation density among the three IoPS templates.

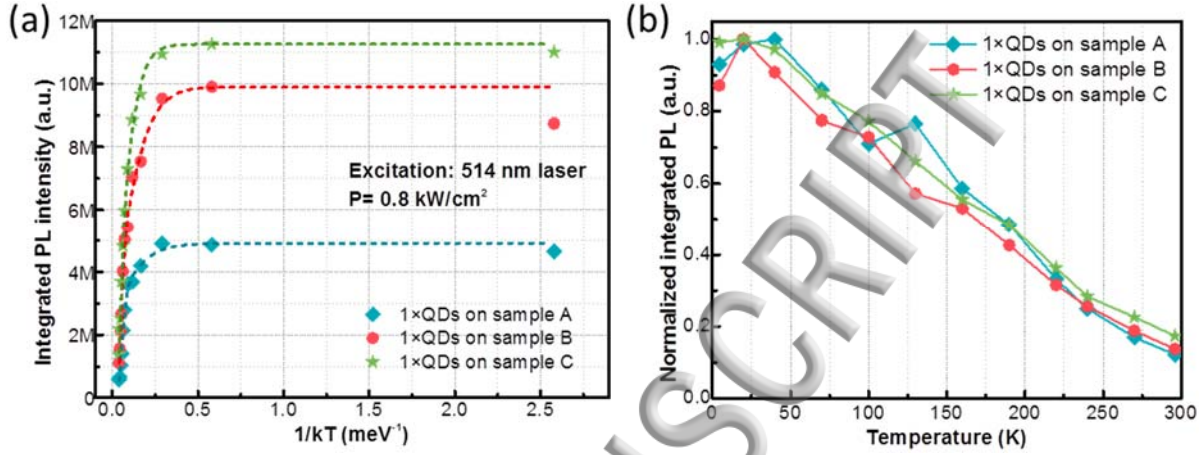


FIG. 12. (a) Integrated PL of QDs on the three samples as a function of temperature. Dashed lines are Arrhenius fitting curves to the measured data; (b) Normalized integrated PL of the three samples to reveal the internal quantum efficiency.

Additionally, we also applied the Arrhenius formula to fit the three sets of IPLI data in Fig.

12(a)²⁹

$$I(T) = \frac{I_0}{1+B_1\left(-\frac{E_{a1}}{kT}\right)+B_2\left(-\frac{E_{a2}}{kT}\right)} \quad (5)$$

where the B_1 , B_2 are fitting coefficients, and E_{a1} , E_{a2} are activation energies, which are related with the carrier capture and escape processes. The extracted E_{a1} , E_{a2} , and IQEs of the samples are summarized in Tab. 3. Here E_{a1} is rather close to the energy separation between QDs ground state and the first excited state, while E_{a2} is related with the escape of electron-hole (e-h) pairs into the wetting layer or InAlGaAs barrier.²⁹ For QDs on sample C, according to the Arrhenius fitting, the activation energy $E_{a1}=19$ meV, which agrees well with the main peak shift from ground state to first excited state (from 1483 nm to 1448 nm, $\Delta E=20$ meV) under high

excitation, as shown in Fig. 11. Moreover, a higher E_{a1} and E_{a2} can be understood in terms of less thermal escape of carriers from QDs ground-state to excited states and wetting layers by non-radiative recombination, influenced by the defect density in the IoPS template that propagated into the InAs/InAlGaAs QD active material. Therefore, for QDs on sample C, the larger E_{a1} and E_{a2} indicate a lower defect density in the InP buffer.

TAB. 3. Activation energies and internal quantum efficiency of the single layer QDs on different samples.

Sample	Activation energy E_{a1} (meV)	Activation energy E_{a2} (meV)	Internal quantum efficiency
1× QDs on sample A	10 ± 4.9	96 ± 9.0	12.2%
1× QDs on sample B	12 ± 3.3	108 ± 13.7	13.7%
1× QDs on sample C	19 ± 5.7	115 ± 20.0	17.3%

The bimodal distribution of the QD sizes on sample C is further investigated via the temperature-dependent PL in Fig. 13. Low excitation was applied to avoid the emergence of excited states. For single layer QDs on sample C, it is noted that two ground-state peaks appear at all the temperature windows, indicating two QD branches. Moreover, at low temperatures, the smaller QDs dominate the luminescence due to the higher emission efficiency with less misfit dislocation generation. As shown in the inset of Fig. 13, the peak energy transition occurs at 100 K, with an energy separation of 44 meV between the two QD peaks.

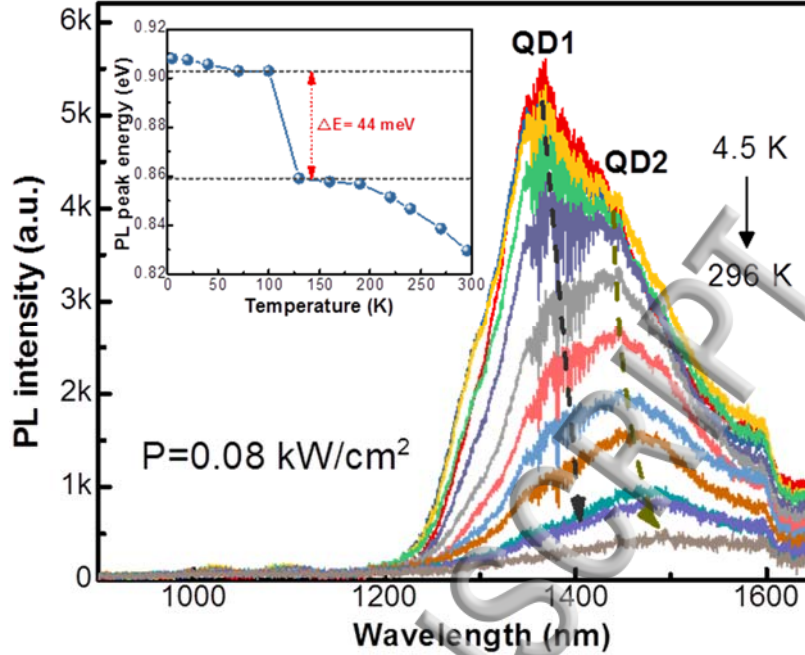


FIG. 13. Temperature-dependent PL of the single layer QDs on sample C at low excitation. Inset shows the extracted peak energy transition as a function of temperature (spectra cutoff beyond 1600 nm).

IV. CONCLUSION

In summary, we have developed and optimized multiple InAs/InP QDs as efficient dislocation filters for InP buffers epitaxially grown on Si substrates. The dislocation filtering effect was comprehensively investigated by XRD, TEM and temperature-dependent PL methods. By capping the QDs with a binary InP layer, a smooth growth front of the dislocation filters can be obtained, minimizing the generation of large InAs islands. A low defect density of $3 \times 10^8 \text{ cm}^{-2}$ was achieved for InP-on-Si with a large QD height of 5 nm according to the statistical plan-view TEM. Furthermore, improved optical property of the QD active layers at both low temperatures and room temperature was obtained on the optimized InP buffer inserted with QD dislocation filters. The larger internal quantum efficiency and higher activation energies verify the effects of the multiple quantum dot dislocation filters. The optimization of quantum dot dislocation filters

offers helpful insights towards the realization of a high quality and smooth InP-on-Si compliant substrate for the low-cost and large-scale silicon photonic integrated circuits.

ACKNOWLEDGEMENTS

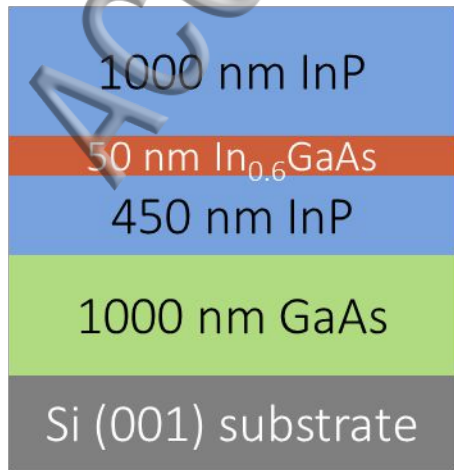
This work was supported in part by Grants (Nos. 614813 and 16212115) from the Research Grants Council of Hong Kong and the Innovation Technology Fund of Hong Kong (No. ITS/273/16FP). The authors would like to thank C. W. Tang for growth assistance, and the Materials Characterization and Preparation Facility of HKUST. Helpful discussions with S. Zhu, B. Lai and Y. Han are also acknowledged.

REFERENCES:

- ¹C. Cornet, Y. Léger, and C. Robert, [Elsevier](#) (2016).
- ²Z. Zhou, B. Yin, and J. Michel, [Light: Sci. Appl.](#) **4**, e358 (2015).
- ³A. W. Fang, H. Park, O. Cohen, R. Jones, M. Paniccia, and J. E. Bowers, [Opt. Express](#) **14**, 9203-9210 (2006).
- ⁴M. Liao, S. Chen, S. Hou, S. Chen, J. Wu, M. Tang, K. Kennedy, W. Li, S. Kumar, M. Martin, T. Baron, C. Jin, I. Ross, A. Seeds, and H. Liu, [IEEE J. Sel. Top. Quant. Electron.](#) **23**, 190910 (2017).
- ⁵D. Jung, P. G. Callahan, B. Shin, K. Mukherjee, A. C. Gossard, and J. E. Bowers, [J. Appl. Phys.](#) **122**, 225703 (2017).
- ⁶J. Yang, P. Bhattacharya, and Z. Mi, [IEEE Trans. Electron Devices](#) **54**, 2849-2855 (2007).
- ⁷S. Chen, W. Li, J. Wu, Q. Jiang, M. Tang, S. Shutts, S. N. Elliott, A. Sobiesierski, A. J. Seeds, I. Ross, P. M. Snowton, and H. Liu, [Nat. Photon.](#) **10**, 307-311 (2016).
- ⁸Y. Wan, J. Norman, Q. Li, M. Kennedy, D. Liang, C. Zhang, D. Huang, Z. Zhang, A. Y. Liu, A. Thorres, D. Jung, A. C. Gossard, E. L. Hu, K. M. Lau, and J. E. Bowers, [Optica](#) **4**, 940-944 (2017).
- ⁹Y. Kohama, Y. Kadota, and Y. Ohmachi, [J. Electrochem. Soc.](#) **136**, 3853-3856 (1989).
- ¹⁰A. Bakin, D. Piester, I. Behrens, H.-H. Wehmann, E. Peiner, A. Ivanov, D. Fehly, and A. Schlachetzki, [Cryst. Growth Des.](#) **3**, 89-93 (2003).
- ¹¹B. Shi, Q. Li, and K. M. Lau, [J. Cryst. Growth](#) **464**, 28-32 (2017).

- ¹²Q. Li, K. W. Ng, C. W. Tang, K. M. Lau, R. Hill, and A. Vert, *J. Cryst. Growth* **405**, 81-86 (2014).
- ¹³M. Paladugu, C. Merckling, R. Loo, O. Richard, H. Bender, J. Dekoster, W. Vandervorst, M. Caymax, and M. Heyns, *Cryst. Growth Des.* **12**, 4696-4702 (2012).
- ¹⁴C. Junesand, H. Kataria, W. Metaferia, N. Julian, Z. Wang, Y.-T. Sun, J. Bowers, G. Pozina, L. Hultman, and S. Lourdudoss, *Opt. Mat. Express* **3**, 1960-1973 (2013).
- ¹⁵D. Kohen, X. S. Nguyen, R. I. Made, C. Heidelberger, K. H. Lee, K. E. K. Lee, and E. A. Fitzgerald, *J. Cryst. Growth* **478**, 64-70 (2017).
- ¹⁶C. W. Tang, Z. Zhong, and K. M. Lau, *ECS Trans.* **28**, 227-231 (2010).
- ¹⁷W. Prost, V. Khorenko, A. Mofor, A. Bakin, E. Khorenko, S. Ehrich, H. -H. Wehmann, A. Schlachetzki, and F.-J. Tegude, *Proceedings of ESSDERC* 257-260 (2005).
- ¹⁸B. Shi, Q. Li, Y. Wan, K. W. Ng, X. Zou, C. W. Tang, and K. M. Lau, *IEEE Photon. Tech. Lett.* **27**, 748-751 (2015).
- ¹⁹M. Khoury, A. Courville, B. Poulet, M. Teisseire, E. Beraudo, M. J. Rashid, E. Frayssinet, B. Damilano, F. Semond, O. Tottereau, and P. Venegues, *Semicond. Sci. Tech.* **28**, 035006 (2013).
- ²⁰Q. Li, C. W. Tang, and K. M. Lau, *Appl. Phys. Express* **7**, 045502 (2014).
- ²¹J. Yang, *Diss. U. Michigan* (2008).
- ²²S. Luo, H.-M. Ji, X.-G. Yang, and T. Yang, *J. Cryst. Growth* **375**, 100-103 (2013).
- ²³S. Banyoudeh, and J. P. Reithmaier, *J. Cryst. Growth* **425**, 299-302 (2015).
- ²⁴B. Shi, and K. M. Lau, *J. Cryst. Growth* **433**, 19-23 (2016).
- ²⁵N. A. Kalyuzhnyy, S. A. Mintairov, R. A. Saliy, A. M. Nadtochiy, A. S. Payusov, P. N. Brunkov, V. N. Nevedomsky, M. Z. Shvarts, A. Martí, V. M. Andreev, and A. Luque, *Prog. Photovolt: Res. Appl.* **24**, 1261-1271 (2016).
- ²⁶B. Shi, S. Zhu, Q. Li, C. W. Tang, Y. Wan, E. L. Hu, and K. M. Lau, *Appl. Phys. Lett.* **110**, 121109 (2017).
- ²⁷J. S. Kim, C. R. Lee, I. H. Lee, J. Y. Leem, J. S. Kim, and M. Y. Ryu, *J. Appl. Phys.* **102**, 073501 (2007).
- ²⁸Z. Gacevic, A. Das, J. Teubert, Y. Kotsar, P. K. Kandaswamy, Th. Kehagias, T. Koukoulas, Ph. Komninou, and E. Monroy, *J. Appl. Phys.* **109**, 103501 (2011).
- ²⁹N. A. Jahan, C. Hermannstadter, J. H. Huh, H. Sasakura, T. J. Rotter, P. Ahirwar, G. Balakrishnan, K. Akahane, M. Sasaki, H. Kumano, and I. Suemune, *J. Appl. Phys.* **113**, 033506 (2013).

(a)

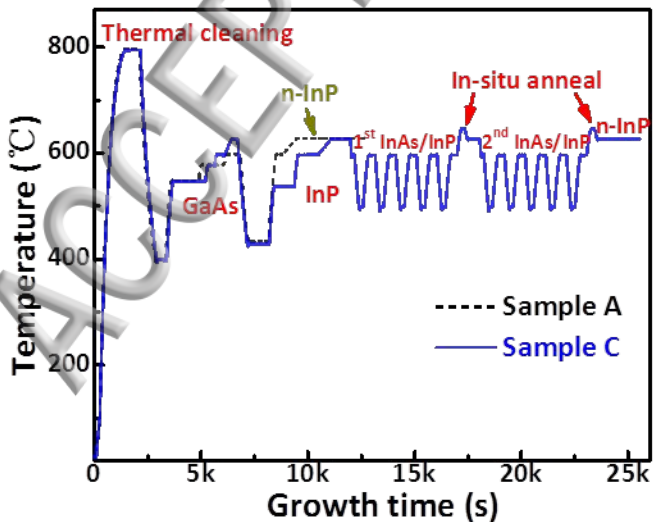


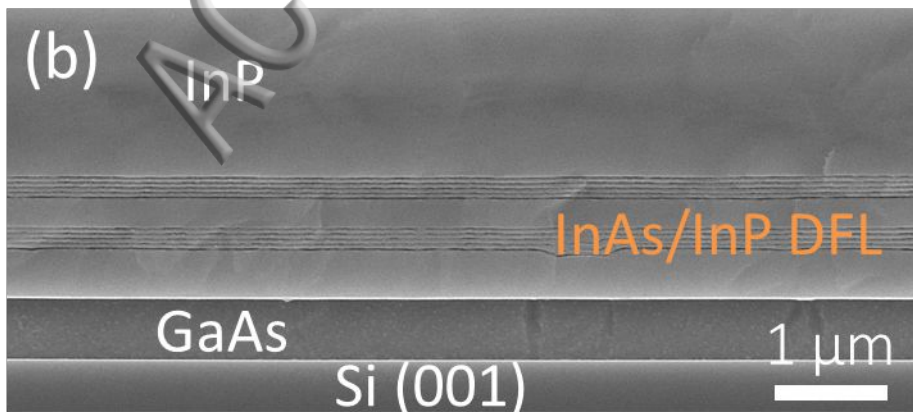
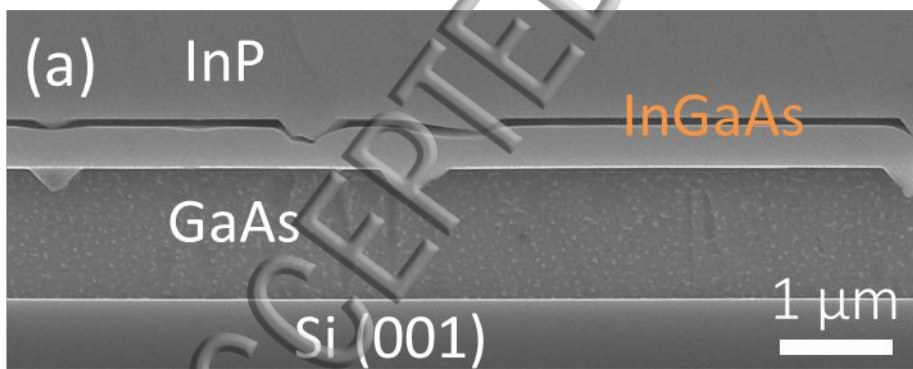
(b)



(c)







(a) RMS=4.60 nm



Pinholes

2 μm

(b) RMS=2.88 nm

SFs

2 μm

45 nm



0 nm

